

Far-field emission profiles from L3 photonic crystal cavity modes

Cristian Bonato,¹ Jenna Hagemeyer,² Dario Gerace,³ Susanna M. Thon,^{2,*} Hyochul Kim,^{2,†}
Lucio C. Andreani,³ Pierre Petroff,² Martin P. van Exter,¹ and Dirk Bouwmeester^{1,2}

¹*Huygens Laboratory, Leiden University, P.O. Box 9504, 2300 RA Leiden, the Netherlands*

²*University of California Santa Barbara, Santa Barbara, California 93106, USA*

³*Dipartimento di Fisica "Alessandro Volta", Università di Pavia, via Bassi 6, 27100 Pavia, Italy*

We experimentally characterize the spatial far-field emission profiles for the two lowest confined modes of a photonic crystal cavity of the L3 type, finding a good agreement with FDTD simulations. We then link the far-field profiles to relevant features of the cavity mode near-fields, using a simple Fabry-Perot resonator model. The effect of disorder on far-field cavity profiles is clarified through comparison between experiments and simulations. These results can be useful for emission engineering from active centers embedded in the cavity.

PACS numbers:

I. INTRODUCTION

Photonic crystals (PhC) offer unprecedented control over electromagnetic field confinement in all three spatial directions [1]. In particular, two-dimensional PhC nanocavities in a planar waveguide have already found applications in different fields such as nanolasers, nonlinear optics and quantum information processing [2, 3]. Similar to any electromagnetic resonator, PhC nanocavity modes are essentially characterized by two figures of merit: the cavity quality factor, Q , and the effective confinement volume of each mode, V_{mode} [4]. The quality factor is proportional to the photon lifetime in the cavity which depends on the cavity losses to the external world. The mode volume is a quantitative measure of the spatial confinement of the electromagnetic mode. In most applications, it is crucial to maximize the Q/V_{mode} ratio. For example, the Purcell factor, which measures the enhancement of the spontaneous emission rates for atoms resonant with a cavity is directly proportional to this figure of merit. In PhC nanocavities the mode is strongly confined to a very small volume, on the order of $(\lambda/n)^3$, where λ is the mode wavelength. In a planar membrane nanocavity, in-plane confinement is provided by spatial localization of a structural defect in a perfectly periodic PhC with a photonic band-gap, while out-of-plane confinement is given by total internal reflection between the slab and the air cladding (assuming a suspended membrane as a planar waveguide). Very high quality factors, in the range 10^4 - 10^6 [5–7] have been demonstrated in the literature. In particular, the L3-type cavity, consisting of three missing holes in a triangular lattice, was the first PhC cavity to show quality factors larger than 10^4 [5].

The spectral mode structure for L3 cavities has been

thoroughly investigated by Chalcraft and coworkers [8] who compared the calculated resonant energies, quality factors and emission polarizations for the lowest-order modes with experimental data. Most experiments coupling single quantum dot emitters to a nanocavity exploit the fundamental (i.e. lowest-energy) cavity mode [9, 10]. However, higher order modes can still be important for, e.g., efficient pumping in nanocavity lasers [11], selective excitation of quantum dots embedded within the cavity [12, 13], or mutually coupling quantum dots in different spatial positions [14]. Several groups have studied the near-field emission profiles of photonic crystal nanocavities [15, 16], even with polarization-resolving imaging [17].

In this paper we report an experimental and theoretical investigation of the spatial far-field profile of the out-of-plane emission for the two lowest-order modes of L3-type PhC nanocavities. We believe the characterization of the out-of-plane far-field emission for PhCs is important for two main reasons. First, for single-photon source applications the emitted radiation needs to be efficiently collected into a fiber, and simultaneous optimization of far-field emission for multiple nanocavity resonances could be useful. In addition, in the case of cavity-QED experiments in the “one-dimensional atom” approximation, a perfect mode-matching is needed to get a large enough interference between the input light field and the field radiated by the atom [18–20]. Recently, quite some work has been done to get a beam-like vertical emission from PhC nanocavities [21–24] for the fundamental mode. Here we extend previous work by experimentally analyzing the far-field emission properties of both the fundamental and the second-order mode, finding good agreement with numerical simulations. We introduce a simple model, based on a one-dimensional Fabry-Perot resonator, to estimate the essential far-field characteristics of a given near-field mode profile and link them to the relevant device parameters. We believe that such a model can be useful for fast parameter optimization, while full-scale numerical simulations can provide an accurate but time-consuming description of the electromagnetic field in the structure. Finally, we will discuss the effect of fabrication imper-

*Current Address: Department of Electrical and Computer Engineering, University of Toronto, 10 King’s College Road, Toronto, Ontario M5S 3G4, Canada

†Current Address: Department of ECE, IREAP, University of Maryland, College Park, Maryland 20742, USA

fections on the far-field cavity emission profiles. As we will show, measurements of far-field profiles are relatively easy to perform and they can provide insightful information about the parameters and the quality of the cavities under examination.

The paper is organized as follows: in Section II, we present experimental measurements of the far-field profiles and a comparison with theoretical far-fields extracted from finite-difference-time-domain (FDTD) simulations; in Section III, we introduce a simple model, based on a Fabry-Perot resonator, which is sufficient to give indications of what the actual far-field profile looks like for a given near-field and to link far-field properties to actual device parameters.

II. THEORETICAL MODELING AND EXPERIMENTAL DATA

Our sample consists of a 180 nm GaAs membrane grown by molecular beam epitaxy on top of a $0.92 \mu\text{m}$ $\text{Al}_{0.7}\text{Ga}_{0.3}\text{As}$ sacrificial layer on a GaAs substrate. An $\text{In}_{0.4}\text{Ga}_{0.6}\text{As}$ quantum dot layer is grown at the center of the GaAs membrane by depositing 10 periods of 0.55 Å-thick InAs and 1.2 Å-thick $\text{In}_{0.13}\text{Ga}_{0.87}\text{As}$. The L3 PhC cavities were fabricated on the sample using standard electron beam lithography and reactive ion etching techniques [25, 26]. The lattice constant of the triangular hole lattice is $a = 240$ nm. The L3 cavity design was properly modified for Q optimization (see modified holes in Fig. 1) [27, 28].

The sample was placed in a He-flow cryostat at about 5 K and illuminated above the GaAs bandgap with a few mW laser beam (wavelength 780 nm) on a few μm^2 spot. The photoluminescence from the quantum dot layer embedded in the membrane was collected in the direction normal to the membrane using a microscope objective with numerical aperture $NA = 0.8$ and spectrally analyzed with a spectrometer (resolution 5.5 GHz/pixel). An example of the spectral emission is shown in Fig. 1 for a device with $R = 54$ nm. According to theoretical predictions based on a guided-mode expansion method [29], the cavity supports two confined modes, with resonances respectively at $\lambda_1^{(th)} = 987$ nm (theoretical Q -factor $Q_{th} \sim 180000$) and $\lambda_2^{(th)} = 957$ nm ($Q_{th} \sim 15000$). Experimentally, we measured the first-order mode with a Lorentzian profile centered around $\lambda_1 = 982.5$ nm with a full-width at half-maximum (FWHM) of 0.195 ± 0.002 nm, from which we extract an experimental quality factor of $Q \sim 5000$. On the other hand, the second-order mode has a less perfect Lorentzian lineshape centered around $\lambda_2 = 956.4$ nm with FWHM 0.63 ± 0.03 nm, and an experimental Q -factor $Q \sim 1500$. Experimental quality factors are lower than the predicted ones due to scattering from fabrication imperfections [30] and possible absorption from sub-bandgap trap levels and surface states [31].

Experimentally, the emitted radiation collected from

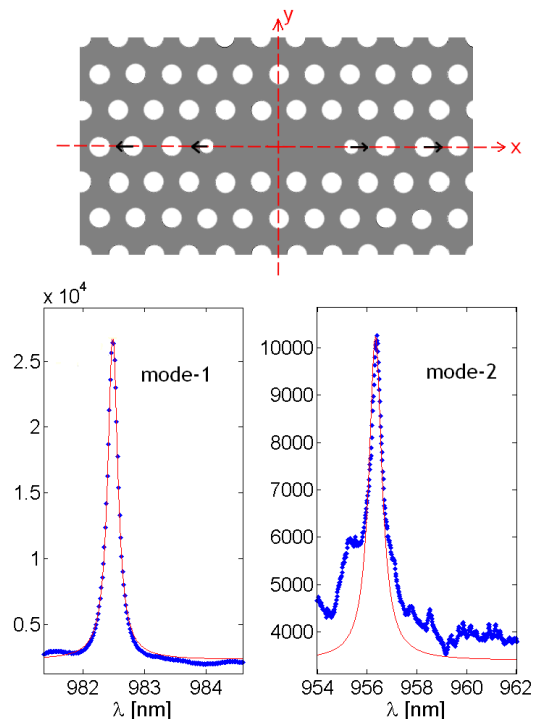


FIG. 1: Top: sketch of the L3 photonic crystal cavity used in the experiments. Given a design radius R for the holes, the two holes closest to and in-line with the cavity have reduced design radii $R' = 0.75R$ [27]. The small holes are shifted from their lattice positions out from the center of the cavity by a fixed quantity (55 nm). Finally, the third holes (i.e. two holes away from the small holes) are shifted from their lattice positions out from the center of the cavity by 45 nm [28], to further increase the theoretical Q . Bottom: experimentally measured photoluminescence spectra for the two cavity modes.

both modes results in a strongly linearly polarized signal. However, as it is shown in the 3D FDTD simulations of Fig. 2, each near-field mode profile has x- and y-components of the electric field of comparable intensity. The reason for the detection of linearly polarized light can be found by calculating the far-field projections of such polarization-resolved near-field profiles.

The far-field profile can be obtained from the near-field using the procedure introduced by Vuckovic and coworkers [32]. According to the surface equivalence theorem, all the information about the far-field profile can be obtained from equivalent electric and magnetic currents, $\mathbf{J}_s = \mathbf{n} \times \mathbf{H}$ and $\mathbf{M}_s = -\mathbf{n} \times \mathbf{E}$, which depend on the in-plane near field components:

$$\begin{aligned} N_x &= -FT_2(H_y) & N_y &= FT_2(H_x) \\ L_x &= FT_2(E_y) & L_y &= -FT_2(E_x) \end{aligned} \quad (1)$$

where FT_2 denoted the two-dimensional Fourier transform. These equivalent currents are used to calculate the retarded vector potential of the electromagnetic field, which in the far-field can be related to Fourier transforms of the near-fields. The radiation intensity per unit solid

angle can be calculated as:

$$K(\theta, \varphi) = \frac{\eta}{8\lambda^2} \left(\left| N_\theta + \frac{L_\varphi}{\eta} \right|^2 + \left| N_\varphi - \frac{L_\theta}{\eta} \right|^2 \right) \quad (2)$$

where $\eta = \sqrt{\mu_0/\epsilon_0}$ is the impedance of free-space and λ is the mode wavelength. The radiation vectors in spherical coordinates can be expressed from their cartesian components as:

$$\begin{aligned} N_\theta &= (N_x \cos \varphi + N_y \sin \varphi) \cos \theta \\ N_\varphi &= -N_x \sin \varphi + N_y \cos \varphi, \end{aligned} \quad (3)$$

and similarly for \mathbf{L} . The far-field profiles calculated from the near-fields in the left panels of Fig. 2 are shown in the same figure, on the right. In these plots, the color scale is normalized to the totally emitted power in the upper half-space of the PhC cavity (the same normalization factor is used for E_x and E_y). Most of the emission from the x-polarization of both modes is predicted at very large angles, and therefore is inefficiently collected by commonly employed microscope objectives. This results in the strong linear polarization observed in the photoluminescence spectra.

To perform a direct measurement of the far-field emitted intensity at each resonant mode frequency, the filtered photoluminescence at the back focal plane of the microscope objective is imaged. Given a characteristic size of the near-field emission, $p \sim 500$ nm, at a wavelength $\lambda \sim 1$ μm the Fresnel number is $F = p^2/(L\lambda) \sim 0.01$, well in the far-field regime ($L \sim 2$ mm). The far-field was imaged on an intensified CCD camera by a lens with focal length 40 cm in a $2f - 2f$ configuration. To make sure that we were looking at the microscope objective back focal plane, we adjusted the lens to see the sharp image of the objective edge on the CCD. This sharp edge was used to calibrate the numerical aperture scale of the far-field images, assuming that the sharp edges correspond to the $NA = 0.8$ of the objective employed. An interference filter, with a bandwidth 1 nm, was used to spectrally select the mode of interest. Images were collected after integrating for 30 s and the background noise was removed by subtracting an image taken with a slightly tilted interference filter.

The experimental far-field spatial emission profiles for the first-order and second-order modes are shown in the two larger plots on the right side of Fig. 3, together with the far-field projections obtained from FDTD simulations (smaller insets on the left) for a direct comparison. The first-order mode exhibits a centrally illuminated area extending to about $NA \sim 0.5$, with a ring-like structure inside ($NA \sim 0.2$), matching the low-NA portion of the simulated far-field. The simulated far-field suggests that most of the light from the first-order mode is emitted in two high-NA lobes, which are not collected at all by our set-up. The far-field profile for the second-order mode consists of two lobes, whose center is at a minimal $NA \sim 0.3$.

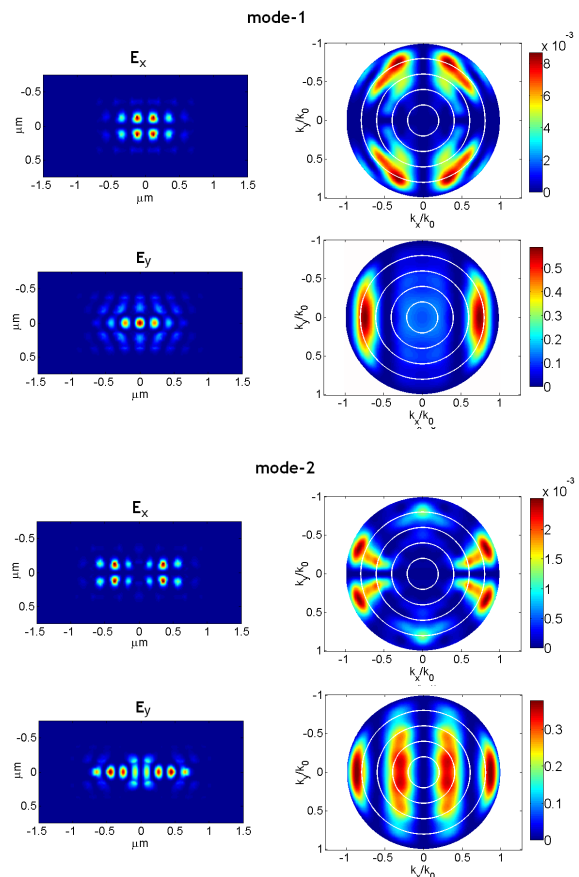


FIG. 2: FDTD simulations of polarization resolved near-field patterns (left panels) and far-field emission profiles (right panels) for the first and second modes of an L3 cavity. Each mode has two linearly-polarized components. The white concentric rings correspond to a grid with numerical-aperture step of 0.2. For far-field plots, the color scale is normalized to the totally emitted power in the upper half-space of the PhC cavity (the same normalization factor is used for E_x and E_y). For the x-polarization, most of the far-field emission is at large angles, making collection less efficient than for y-polarization and resulting in a strongly polarized photoluminescence signal.

Finer details also appear inside the two lobes, in the form of spots separated by $\Delta k/k_0 \sim 0.1 - 0.2$. Such structures correspond, in the near-field, to light sources which are separated from the cavity about 5 – 10 times the characteristic size of the cavity mode. The simulated near-field profiles shown in Fig. 2 suggest that the optical field decays very fast out of the cavity region, implying that such features might be due to light that escapes from the cavity due to fabrication imperfections [30]. The fine details are reproducible for different measurements performed on the same device. Finally, we show in Fig. 4 the far-field profiles of the second-order modes for different devices on the same wafer. Each plot shows the characteristic two-lobes profile, as expected for this mode, with reproducible finer details that appear to be device-dependent.

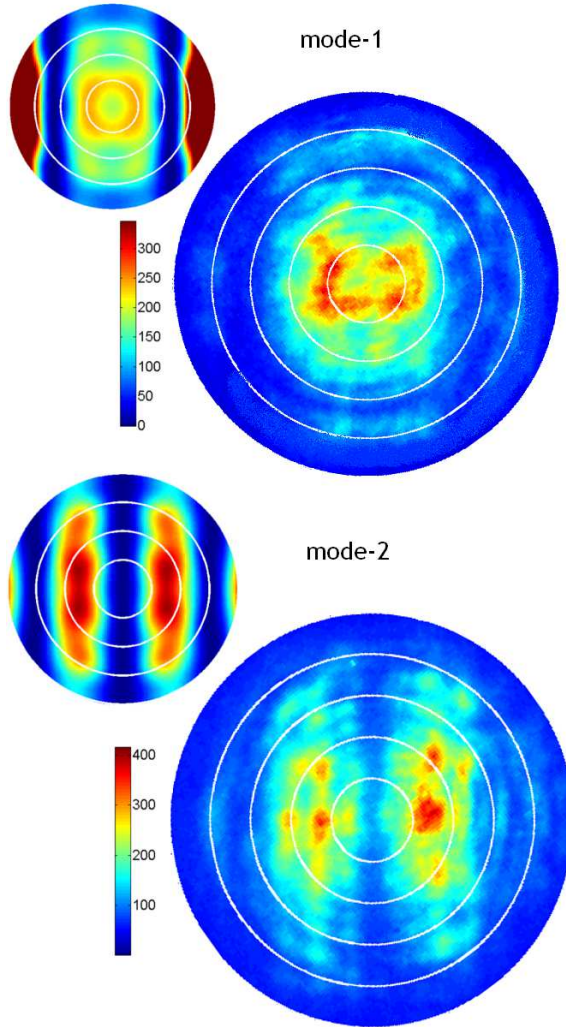


FIG. 3: Experimental far-field emission profiles for the two L3 cavity modes (larger panels) and the corresponding predictions by FDTD simulations (smaller panels on the top left of the experimental plots), resulting from the sum of x - and y -components in Fig. 2. The white concentric rings correspond to a grid with numerical-aperture step of 0.2. The color scale bars show the detected photon counts per second. The counts for the two profiles cannot be compared since they depend not only on the device parameters, but also on the density of quantum dots emitting in the wavelength range of the specific cavity mode.

To investigate the cause of fine structure within the two-lobe far-field pattern of the second order mode, FDTD simulations were done in which disorder was introduced. It is assumed that, due to fabrication imperfections, the dominant type of disorder is in the hole radii of the PhC lattice. Therefore, the hole radii R were varied randomly according to the distribution function $P(R) \propto \exp[-(R - \bar{R})^2/2\sigma^2]$. Some simulation data are given in Figure 5, showing disorder introduced to the far-field profiles as a result of increasing the disorder parameter σ .

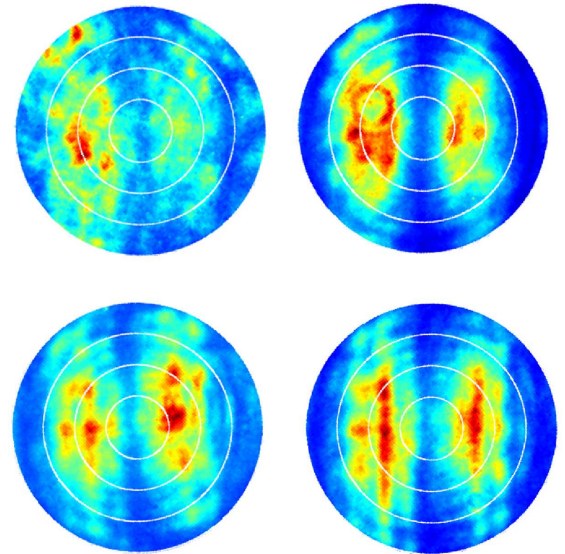


FIG. 4: Experimental far-field profiles of the second-order mode emission from four different devices on the same wafer. Finer details are reproducible in different measurements performed on the same device, but differ from device to device. The white concentric rings correspond to a grid with numerical-aperture step of 0.2.

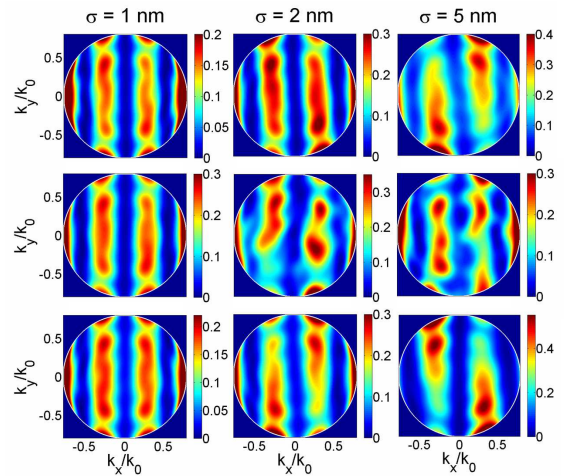


FIG. 5: Far-field intensity profiles for varying degrees of disorder, normalized by the total power radiated into the upper half space. The images are cut-off at a numerical aperture value of 0.8, indicated by the white line, to allow for better comparison with experimental data. Data are shown for disorder parameters of $\sigma = 1$ nm (left column), 2 nm (middle column), and 5 nm (right column).

ter σ . These results indicate that far-field measurements could be used as an indicator of disorder in the lattice structure.

III. A SIMPLE FABRY-PEROT MODEL

In general, 3D FDTD simulations can provide accurate modeling of near-field and far-field properties of PhC cavity modes. However, they give little physical insight on how the detected features of such far-field profiles can be related to specific device parameters. In this Section, we will show that the experimental data can be reproduced by a simple model, elaborated from the proposal of Sauvan and coworkers [33].

For a line of $N \geq 3$ missing holes, the PhC nanocavity can be described quite accurately by a Fabry-Perot resonator, in which the fundamental Bloch mode of a single-line-defect PhC waveguide is trapped between two PhC mirrors of modal reflectivity $r(\lambda)$. The properties of such a cavity are shown to depend only on three parameters, namely the group index n_g of the Bloch mode, the reflection coefficient $r(\lambda)$ of the mirrors and the effective cavity length L . The Bloch mode can be calculated as the eigenstate of the PhC waveguide in the Fourier basis, and its modal reflectivity can be obtained with the method described in Ref. [34]. Fabry-Perot models have been shown to be a useful tool to probe cavity resonances and the group index of photonic crystal waveguides [35, 36], and to describe acousto-mechanical cavity tuning effects [37]. We consider the E_y near-field profiles shown in Fig. 2. Taking the intensity distribution along the $y = 0$ axis, the modes show a sinusoidal intensity distribution with nodes and antinodes in the cavity region, decaying exponentially outside the cavity region. From simulations, the intensity decay length for the first-order mode is $\delta_1 \sim 220 \pm 10$ nm, while it is $\delta_2 \sim 155 \pm 8$ nm for the second-order mode. This is very similar to the intensity distribution in a cavity between two Distributed Bragg Reflectors (DBR). For the E_y near-field profiles most of the radiation is emitted along the $y = 0$ axis, with little structure and weaker intensity outside. Given the relevance of such polarization in determining the far-field emission properties, to a first-order approximation it makes sense to consider a one-dimensional model, which takes into account only the structure along the $y = 0$ axis. Such a model has the advantage of being extremely simple, although able to give significant hints on the main far-field profile properties. A two-dimensional model based on an effective index approximation should be used (with no significant difficulties) to study also the E_x profiles.

Let us consider a one-dimensional Fabry-Perot resonator, with the field intensity profile varying sinusoidally in the cavity region and exponentially decaying in the mirror regions, with characteristic penetration depth δ . The resonant frequency Ω_m can be calculated by imposing the total phase acquired by the Bloch mode traveling back and forth to be a multiple of π . The far-field profile can be calculated using the procedure outlined in the previous Section (Eq. 2). Since the modes are TE-like modes, only E_x , E_y and H_z are non-negligible and only the L_x component is relevant in

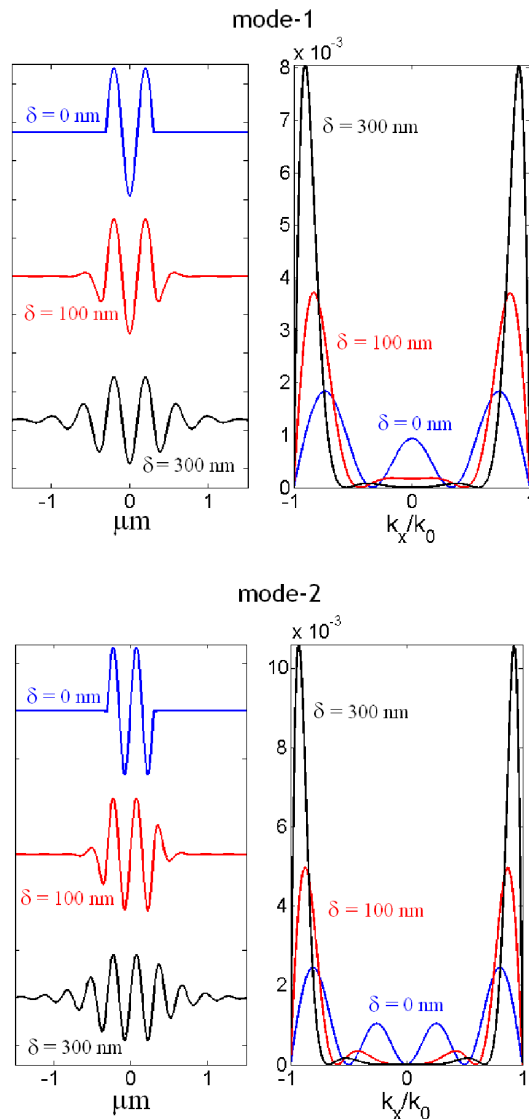


FIG. 6: Far-field results for the one-dimensional Fabry-Perot model (first and second-order modes). For each mode, on the left side the expected near-field profile considering a Fabry-Perot cavity with DBR mirrors with varying penetration depth δ . On the right side, the corresponding far-field profiles calculated from Eq. 4. For the first-order mode, in the region $|k_x|/k_0 < 0.5$, there is a single peak centered at $k_x/k_0 = 0$ for small penetration depth. This peak flattens and broadens on increasing penetration depth. For large enough penetration depth, the central peak splits into two smaller peaks. The second-order mode, in the region $|k_x|/k_0 < 0.5$, consists of two peaks that split further and further out for increasing penetration depth δ .

Eq. 2. Let's consider a separable electric field distribution $E_y(x, y) = \alpha(x)\beta(y)$. The component L_x is separable as well: $L_x = \tilde{\alpha}(k_x)\tilde{\beta}(k_y)$, where $\tilde{\alpha}$ and $\tilde{\beta}$ are the one-dimensional Fourier transforms of $\alpha(x)$ and $\beta(y)$,

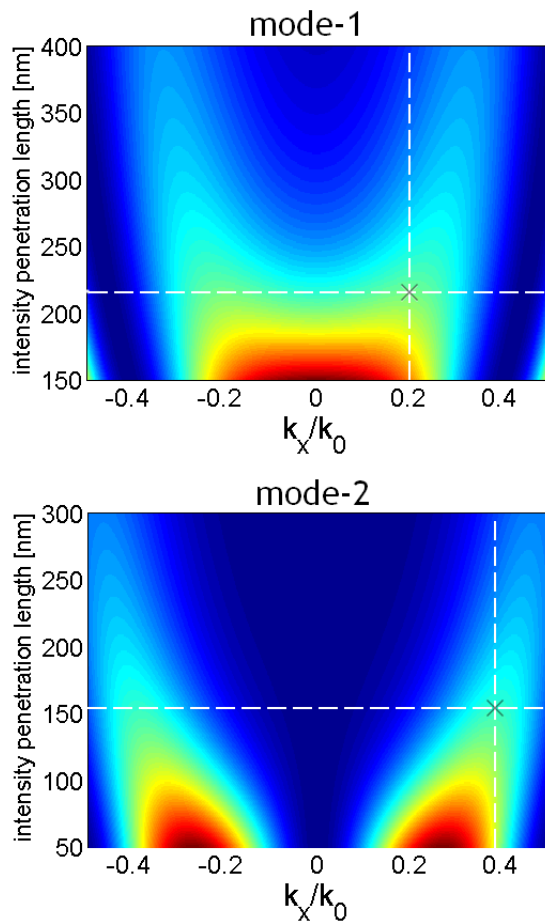


FIG. 7: One-dimensional far-field profiles as a function of the intensity penetration depths calculated using the simple Fabry-Perot model for the first (left-side plot) and the second (right-side plot) order modes. The white dashed lines correspond to the experimental position of the center of the lobes (Fig. 3) and the penetration depth from FDTD simulations.

making:

$$K(\theta, \varphi) \propto |\tilde{\alpha}(k_0 \sin \theta \cos \varphi)|^2 |\tilde{\beta}(k_0 \sin \theta \sin \varphi)|^2 \times (\cos^2 \varphi \cos^2 \theta + \sin^2 \varphi) \quad (4)$$

In a simplified one-dimensional model, $\beta(y)$ is narrow in real-space, so its Fourier transform is wide and can be neglected ($|\tilde{\beta}(k_y)|^2 \sim 1$). If we look at the far-field distribution along the x-axis we select $\varphi = 0$, so that the resulting one-dimensional far-field profile is:

$$K(\theta) \sim |\tilde{\alpha}(k_0 \sin \theta)|^2 \cos^2 \theta \quad (5)$$

or, in terms of transverse wavevectors: $K(k_x) \sim |\tilde{\alpha}(k_x)|^2 (k_0^2 - k_x^2)$.

An analytical solution can be found and is reported in Appendix A. However, the resulting formula is too complicated to give intuitive insights; therefore we will just discuss the numerical results (from Eq. 12) in this context. Fig. 6 shows the expected far-field profiles for

the first and second-order modes for different values of the penetration depth, δ . The first-order mode exhibits a central peak (centered at $k = 0$) and two outer lobes as predicted by the FDTD simulations. We see that, for increasing penetration depth, the two main outer lobes become narrower in k-space and more outward, while the central peak broadens and flattens. A similar behavior can be observed in the second-order mode. Here, the far-field profile is given by two central peaks and two outer lobes, and again, for increasing penetration depth δ the two outer lobes move outwards and become more localized.

The Fabry-Perot resonator model was shown to give results for the quality factor Q in agreement with more sophisticated FDTD simulations [33]:

$$Q = \frac{k_0}{1-R} n_g (L + 2L_p) \quad (6)$$

where the group delay $\tau = \frac{\partial \phi_r}{\partial \omega}$ experienced by the light upon mirror reflection enters as a characteristic length $L_p = -\lambda_0^2 / (4\pi n_g) (\partial \phi_r / \partial \lambda)_{\lambda_0}$. In general, for PhC structures (for example, heterostructure mirrors) it has been shown that L_p can be unrelated to the characteristic damping length of the energy distribution inside the mirrors δ [38]. However, in the configuration under investigation, the classical relation for a DBR, $L_p \leq \delta$, is valid, with the equality being strictly fulfilled only in the limiting case of quarter-wave mirrors with low refractive index contrast, $\Delta n/n$ ($L_p = \delta = n\Lambda / (2\Delta n)$).

In Fig. 7, the emission in the region $|k_x/k_0| < 0.5$ is shown as a function of the penetration depth. In the case of the fundamental mode, there is a single peak centered around $k = 0$ for small penetration depth, with a quite flat profile and broadening for $|k_x/k_0| < 0.25$. When the penetration depth increases beyond $\delta \sim 150$ nm, the far-field emission splits into two lobes, which separate more and more on increasing δ . At $\delta \sim 250$ nm, the peaks are centered around $k \sim \pm 0.25k_0$, corresponding to an opening angle of about 15 degrees. These findings explain the ring-like structure we observe in the experimental far-field: the vertical dashed white line in the figure shows the experimental central NA for the peaks (from Fig. 3), which corresponds to a penetration depth of about 220 nm, fully compatible with the penetration depth from FDTD simulations, δ_1 . For the second-order mode, in the region $|k_x/k_0| < 0.5$ there are always two emission lobes, even at small penetration depth. On increasing δ , the two lobes move further and further apart. From Fig. 3, the lobes are centered around $NA \sim 0.35$, which in our simulations is consistent with a penetration depth of about 150 nm, as predicted by FDTD simulations. Therefore, far-field profiles can provide useful information about the penetration depth δ of PhC cavity modes, which in this case offer a bound on the effective cavity length, L_p , and therefore on the Q-factor. Extensions of the present analysis to treat coupled cavity modes [39, 40] can also be considered.

IV. CONCLUSIONS

In conclusion, we have presented an extensive characterization of far-field emission profiles from L3-type photonic crystal nanocavities, introducing a simple imaging technique as an efficient tool to give a two-dimensional mapping of the emitted intensity. The measurements have been directly compared to theoretically modeled far-field projections from the 3D FDTD near-field cavity modes profiles, and we believe these results to be useful to PhC cavity designs for specific purposes. The effect of disorder on the far-field profiles was investigated via numerical simulations.

Finally, we have introduced a simple Fabry-Perot model that is able to capture the essential features of far-field properties for suitably designed near-field profiles. As a particular application of this model, we can envision, for example, the simultaneous optimization of in- and out-coupling for two different modes supported by the same PhC cavity, which is still an open problem that might benefit from simplified models like the one presented here.

Acknowledgments

The authors acknowledge helpful discussions with Morten Bakker. This work was supported by NSF NIRT Grant No. 0304678, Marie Curie EXT-CT-2006-042580 and FOM\NWO grant No. 09PR2721-2. A portion of this work was done in the UCSB nanofabrication facility, part of the NSF funded NNIN network.

Appendix A: Analytical calculations

The resonance frequencies for the modes can be found by setting the condition that the total phase acquired by the Bloch mode traveling back and forth is a multiple of π ($2k_m L = m\pi$), which results in:

$$k_m = \frac{m\pi}{2L} \quad (7)$$

Let us start with a perfectly confined mode, with no penetration into the mirrors ($\delta = 0$). In this case the field is given by:

$$\alpha_{\delta=0}(x) = \Pi\left(\frac{x}{L}\right) e^{i(k_m x + \phi_m)} + \text{c. c.} \quad (8)$$

where $\Pi(x)$ is the rectangular function, $\Pi(x) = 1$ for $|x| < 1/2$ and zero elsewhere. The phase ϕ_m is set by the boundary conditions: $\phi_m = 0$ for m even (cosine-like solutions) and $\phi_m = \pi/2$ for m odd (sine-like solutions). From Eq. 4:

$$K_1(\theta) \sim \left| e^{i\phi_m} \text{Sinc}\left[\frac{m\pi}{2}(\sin\theta - 1)\right] + e^{-i\phi_m} \text{Sinc}\left[\frac{m\pi}{2}(\sin\theta + 1)\right] \right|^2 \cos^2\theta \quad (9)$$

The two modulo-squared Sinc functions in Eq. 9 give two main peaks centered at $\theta = \pm\pi/2$, which correspond to the higher-NA peaks in the far-field in Fig. 6. The first relative maximum of $\text{Sinc}^2(x)$ is at $x \sim 1.4303\pi$, which for Eq. 9 corresponds to $\sin\theta \sim \pm(1 - 2.861/m)$. The FWHM of such a peak for $\text{Sinc}^2(x)$ is 0.522π , which corresponds to $\delta k_x \sim 1.044/m$ ($\delta k_x \sim 0.35$ for the first-order mode, corresponding to $m = 3$, and $\delta k_x \sim 0.26$ for the second-order mode, corresponding to $m = 4$). Therefore for the first-order mode, the first relative maxima of the Sinc functions superpose, giving just one central peak. For the second-order mode, on the other hand, the first relative maxima are well separated.

Including the penetration depth δ into the model, a simple near-field profile can be taken as a superposition of $\Pi\left(\frac{x}{L}\right)$ and two exponentially-decaying wings, as follows:

$$\alpha(x) = \left[\Pi\left(\frac{x}{L}\right) + H\left(x - \frac{L}{2}\right) e^{-(x-L/2)/\delta} + H\left(-x - \frac{L}{2}\right) e^{-(x-L/2)/\delta} \right] e^{i(k_m x + \phi_m)} + \text{c. c.} \quad (10)$$

where $H(x)$ is the Heaviside function ($H(x) = 1$ for $x > 0$, $H(x) = 0$ for $x < 0$). The part around $x = 0$ ($\Pi\left(\frac{x}{L}\right)$) gives the same Fourier-transform as in Eq. 9 (which we label $\tilde{\alpha}_1(\sin\theta)$), while the left and right-side exponential decay regions give the following:

$$\begin{aligned} \tilde{\alpha}_2(\sin\theta) &\sim e^{i\phi_m} \frac{e^{im(\pi/2)(\sin\theta+1)}}{\delta/L - im\pi(\sin\theta+1)} + e^{-i\phi_m} \frac{e^{im(\pi/2)(\sin\theta-1)}}{\delta/L - im\pi(\sin\theta-1)} \\ \tilde{\alpha}_3(\sin\theta) &\sim e^{i\phi_m} \frac{e^{-im(\pi/2)(\sin\theta\pm 1)}}{\delta/L + im\pi(\sin\theta\pm 1)} + e^{-i\phi_m} \frac{e^{-im(\pi/2)(\sin\theta-1)}}{\delta/L + im\pi(\sin\theta-1)} \end{aligned} \quad (11)$$

All the quantities depend on the ratio δ/L between the penetration depth and the cavity length. The far-field profile can be calculated to be:

$$K_1(\theta) = \left| \sum_{j=1}^3 \tilde{\alpha}_j(\sin\theta) \right|^2 \cos^2\theta \quad (12)$$

-
- [1] J. D. Joannopoulos, S. G. Johnson, J. N. Winn, R. D. Meade, *Photonic Crystals: Molding the Flow of Light*, Princeton University Press, 2 edition, 2008.
[2] P. Yao, V. Manga Rao, S. Hughes, On-chip single photon sources using planar photonic crystals and single quantum dots, *Laser & Photonics Reviews* 4 (2010) 499–516.
[3] J. L. O’Brien, A. Furusawa, J. Vuckovic, Photonic quan-

- tum technologies, *Nat Photon* 3 (2009) 687–695.
[4] M. Notomi, Manipulating light with strongly modulated photonic crystals, *Reports on Progress in Physics* 73 (2010) 096501.
[5] Y. Akahane, T. Asano, B. Song, S. Noda, High-Q photonic nanocavity in a two-dimensional photonic crystal, *Nature* 425 (2003) 944–947.

- [6] B. Song, S. Noda, T. Asano, Y. Akahane, Ultra-high-Q photonic double-heterostructure nanocavity, *Nat Mater* 4 (2005) 207–210.
- [7] E. Kuramochi, M. Notomi, S. Mitsugi, A. Shinya, T. Tanabe, T. Watanabe, Ultrahigh-q photonic crystal nanocavities realized by the local width modulation of a line defect, *Appl. Phys. Lett.* 88 (2006) 041112.
- [8] A. R. A. Chalcraft, S. Lam, D. O’Brien, T. F. Krauss, M. Sahin, D. Szymanski, D. Sanvitto, R. Oulton, M. S. Skolnick, A. M. Fox, D. M. Whittaker, H.-Y. Liu, M. Hopkinson, Mode structure of the l3 photonic crystal cavity, *Applied Physics Letters* 90 (2007) 241117.
- [9] S. Strauf, K. Hennessy, M. T. Rakher, Y.-S. Choi, A. Badolato, L. C. Andreani, E. L. Hu, P. M. Petroff, D. Bouwmeester, Self-tuned quantum dot gain in photonic crystal lasers, *Physical Review Letters* 96 (2006) 127404.
- [10] K. Hennessy, A. Badolato, M. Winger, D. Gerace, M. Atatüre, S. Gulde, S. Fält, E. L. Hu, A. Imamoglu, Quantum nature of a strongly coupled single quantum dotcavity system, *Nature (London)* 445 (2007) 896–899.
- [11] M. Nomura, S. Iwamoto, M. Nishioka, S. Ishida, Y. Arakawa, Highly efficient optical pumping of photonic crystal nanocavity lasers using cavity resonant excitation, *Applied Physics Letters* 89 (2006) 161111.
- [12] M. Nomura, S. Iwamoto, T. Yang, S. Ishida, Y. Arakawa, Enhancement of light emission from single quantum dot in photonic crystal nanocavity by using cavity resonant excitation, *Applied Physics Letters* 89 (2006) 241124.
- [13] R. Oulton, B. D. Jones, S. Lam, A. R. A. Chalcraft, D. Szymanski, D. O’Brien, T. F. Krauss, D. Sanvitto, A. M. Fox, D. M. Whittaker, M. Hopkinson, M. S. Skolnick, Polarized quantum dot emission from photonic crystal nanocavities studied under moderesonant enhanced excitation, *Opt. Express* 15 (2007) 17221–17230.
- [14] A. Imamoglu, S. Fält, J. Dreiser, G. Fernandez, M. Atatüre, K. Hennessy, A. Badolato, D. Gerace, Coupling quantum dot spins to a photonic crystal nanocavity, *Journal of Applied Physics* 101 (2007) 081602.
- [15] S. Mujumdar, A. F. Koenderink, T. Süner, B. C. Buchler, M. Kamp, A. Forchel, V. Sandoghdar, Near-field imaging and frequency tuning of a high-q photonic crystal membrane microcavity, *Opt. Express* 15 (2007) 17214–17220.
- [16] F. Intonti, S. Vignolini, F. Riboli, A. Vinattieri, D. S. Wiersma, M. Colocci, L. Balet, C. Monat, C. Zinoni, L. H. Li, R. Houdré, M. Francardi, A. Gerardino, A. Fiore, M. Gurioli, Spectral tuning and near-field imaging of photonic crystal microcavities, *Phys. Rev. B* 78 (2008) 041401.
- [17] S. Vignolini, F. Intonti, F. Riboli, D. S. Wiersma, L. Balet, L. H. Li, M. Francardi, A. Gerardino, A. Fiore, M. Gurioli, Polarization-sensitive near-field investigation of photonic crystal microcavities 94 (2009) 163102.
- [18] E. Waks, J. Vuckovic, Dipole induced transparency in drop-filter cavity-waveguide systems, *Phys. Rev. Lett.* 96 (2006) 153601.
- [19] A. Auffèves-Garnier, C. Simon, J.-M. Gerard, J.-P. Poizat, Giant optical nonlinearity induced by a single two-level system interacting with a cavity in the Purcell regime, *Phys. Rev. A* 75 (2007) 053823.
- [20] C. Bonato, F. Haupt, S. S. R. Oemrawsingh, J. Gudat, D. Ding, M. P. van Exter, D. Bouwmeester, and bell-state analysis in the weak-coupling cavity qed regime, *Phys. Rev. Lett.* 104 (2010) 160503.
- [21] S.-H. Kim, S.-K. Kim, Y.-H. Lee, Vertical beaming of wavelength-scale photonic crystal resonators, *Phys. Rev. B* 73 (2006) 235117.
- [22] N.-V.-Q. Tran, S. Combré, A. De Rossi, Directive emission from high- q photonic crystal cavities through band folding, *Phys. Rev. B* 79 (2009) 041101.
- [23] M. Toishi, D. Englund, A. Faraon, J. Vučković, High-brightness single photon source from a quantum dot in a directional-emission nanocavity, *Opt. Express* 17 (2009) 14618–14626.
- [24] S. L. Portalupi, M. Galli, C. Reardon, T. Krauss, L. O’Faolain, L. C. Andreani, D. Gerace, Planar photonic crystal cavities with far-field optimization for high coupling efficiency and quality factor, *Opt. Express* 18 (2010) 16064–16073.
- [25] A. Badolato, K. Hennessy, M. Atature, J. Dreiser, E. Hu, P. M. Petroff, A. Imamoglu, Deterministic coupling of single quantum dots to single nanocavity modes, *Science* 308 (2005) 1158–1161.
- [26] S. M. Thon, M. T. Rakher, H. Kim, J. Gudat, W. T. M. Irvine, P. M. Petroff, D. Bouwmeester, Strong coupling through optical positioning of a quantum dot in a photonic crystal cavity, *Applied Physics Letters* 94 (2009) 111115.
- [27] L. C. Andreani, D. Gerace, M. Agio, Gap maps, diffraction losses, and exciton-polaritons in photonic crystal slabs, *Photonics and Nanostructures - Fundamentals and Applications* 2 (2004) 103 – 110.
- [28] Y. Akahane, T. Asano, B.-S. Song, S. Noda, Fine-tuned high-q photonic-crystal nanocavity, *Opt. Express* 13 (2005) 1202–1214.
- [29] L. C. Andreani, D. Gerace, Photonic-crystal slabs with a triangular lattice of triangular holes investigated using a guided-mode expansion method, *Phys. Rev. B* 73 (2006) 235114.
- [30] S. L. Portalupi, M. Galli, M. Belotti, L. C. Andreani, T. F. Krauss, L. O’Faolain, Deliberate versus intrinsic disorder in photonic crystal nanocavities investigated by resonant light scattering, *Phys. Rev. B* 84 (2011) 045423.
- [31] C. P. Michael, K. Srinivasan, T. J. Johnson, O. Painter, K. H. Lee, K. Hennessy, H. Kim, E. Hu, Wavelength- and material-dependent absorption in gaas and algaas microcavities, *Applied Physics Letters* 90 (2007) 051108.
- [32] J. Vuckovic, M. Loncar, H. Mabuchi, A. Scherer, Optimization of the q factor in photonic crystal microcavities, *IEEE J. Quant. Electr.* 38 (2002) 850.
- [33] C. Sauvan, P. Lalanne, J. P. Hugonin, Slow-wave effect and mode-profile matching in photonic crystal microcavities, *Phys. Rev. B* 71 (2005) 165118.
- [34] E. Silberstein, P. Lalanne, J.-P. Hugonin, Q. Cao, Use of grating theories in integrated optics, *J. Opt. Soc. Am. A* 18 (2001) 2865–2875.
- [35] S. Combré, E. Weidner, A. DeRossi, S. Bansropun, S. Cassette, A. Talneau, H. Benisty, Detailed analysis by fabry-perot method of slab photonic crystal line-defect waveguides and cavities in aluminium-free material system, *Opt. Express* 14 (2006) 7353.
- [36] P. Lalanne, C. Sauvan, J. Hugonin, Photon confinement in photonic crystal nanocavities, *Laser & Photonics Reviews* 2 (2008) 514–526.
- [37] D. A. Fuhrmann, S. M. Thon, H. Kim, D. Bouwmeester, P. M. Petroff, A. Wixforth, H. J. Krenner, Dynamic mod-

- ulation of photonic crystal nanocavities using gigahertz acoustic phonons, *Nat Photon* 5 (2011) 605–609.
- [38] C. Sauvan, J. P. Hugonin, P. Lalanne, Difference between penetration and damping lengths in photonic crystal mirrors, *Applied Physics Letters* 95 (2009) 211101.
- [39] F. Intonti, F. Riboli, N. Caselli, M. Abbarchi, S. Vignolini, D. S. Wiersma, A. Vinattieri, D. Gerace, L. Balet, L. H. Li, M. Francardi, A. Gerardino, A. Fiore, M. Gurioli, Youngs type interference for probing the mode symmetry in photonic structures, *Physical Review Letters* 106 (2011) 143901.
- [40] M. Brunstein, T. J. Karle, I. Sagnes, F. Raineri, J. Bloch, Y. Halioua, G. Beaudoin, L. L. Gratiet, J. A. Levenson, A. M. Yacomotti, Radiation patterns from coupled photonic crystal nanocavities, *Applied Physics Letters* 99 (2011) 111101.